Research Square

Preprints are preliminary reports that have not undergone peer review.
They should not be considered conclusive, used to inform clinical practice,
or referenced by the media as validated information.

Kinematic modeling and experimental investigation of tool–workpiece separation in ultrasonic vibration-assisted milling of TC11 titanium alloy under scCO$_2$-MQL conditions

Limin Shi

slm@tsnu.edu.cn

Haonan Chen
Lixin Cui
Yifan Zhang
Ronghuan Liu
Nana Li
Deguo Kong

Research Article

Keywords: Ultrasonic vibration-assisted milling, Separation kinematic model, Separation ratio, Effective cooling time, TC11 titanium alloy

Posted Date: November 24th, 2026

DOI: https://doi.org/10.21203/rs.3.rs-11631363/v1

License: This work is licensed under a Creative Commons Attribution 4.0 International License.
Read Full License

Kinematic modeling and experimental investigation of tool–workpiece separation in ultrasonic vibration-assisted milling of TC11 titanium alloy under scCO₂-MQL conditions

Limin Shi*, Haonan Chen, Lixin Cui, Yifan Zhang, Ronghuan Liu,
Nana Li,Deguo Kong
School of Mechanical and Electrical Engineering, Tianshui Normal University,
Tianshui 741000, Gansu, China
*Corresponding author. E-mail: slm@tsnu.edu.cn

Abstract

A tool-workpiece separation kinematic model for ultrasonic vibration-assisted milling (UVAM) of TC11 titanium alloy was established. In this model, the separation ratio (R_s), maximum separation gap (g_{max}), and effective cooling time (t_{cool}) were defined. Theoretical derivation revealed that an increase in feed speed (v_f) resulted in a synchronous decrease in R_s and t_{cool}. This mechanism was jointly validated through finite element simulations and milling experiments. With the increase in cutting speed, the weakened separation effect caused the reduction in cutting force to narrow from 26% to 10%. Meanwhile, the relatively larger R_s facilitated the penetration conditions of the cooling medium, resulting in surface roughness reductions of 55%~42% under the hybrid process. Additionally, the tool wear width at 48 min was significantly reduced to 150.16 μm. The results confirm that R_s can serve as a key dimensionless indicator for evaluating the degree of intermittent cutting in UVAM. The established model provides a theoretical basis for the high-efficiency and precision machining of titanium alloys under scCO₂-MQL conditions.

Keywords: Ultrasonic vibration-assisted milling; Separation kinematic model; Separation ratio R_s; Effective cooling time; TC11 titanium alloy

1 Introduction

TC11 titanium alloy[1–2], an α+β dual-phase titanium alloy with excellent overall performance, is widely used in aerospace owing to its inherent material characteristics,

including low thermal conductivity, low elastic modulus, high strength at elevated temperatures, and high chemical reactivity. However, its machining presents serious challenges: cutting heat is difficult to dissipate, causing a rapid rise in tool temperature[3–4] and severe tool wear[5–6]; chips[7–8] are serrated and difficult to break, leading to poor machining stability; and machined surfaces[9–11] are susceptible to roughness fluctuations, which directly affect the fatigue life of components. To overcome these three problems, researchers have proposed various methods, including the use of coated tools, minimum quantity lubrication (MQL), and ultrasonic vibration-assisted machining.

Coated tools[12–13] are fabricated by depositing a high-hardness synthetic material onto the surface of a conventional tool, thereby enhancing tool hardness without altering the tool's overall integrity; however, during milling, the coating still tends to spall owing to excessively high temperatures generated in the machining process. Minimum quantity lubrication (MQL)[14–15] uses high pressure to atomize cutting fluid into droplets and a high-pressure air stream to deliver these droplets more precisely to the cutting zone; nevertheless, the cutting zone remains enclosed and is difficult to access, and the atomized droplets are heated to form an "air barrier" that partially isolates them, ultimately preventing the desired effect from being achieved. Ultrasonic vibration-assisted machining[16–17] has thus emerged, converting the continuous cutting process into intermittent cutting motion, which enables the cutting fluid to better enter the cutting zone and thereby enhances heat dissipation from the enclosed cutting region.

Numerous experimental and theoretical studies on ultrasonic vibration technology have been conducted by researchers worldwide. These studies indicate that ultrasonic vibration-assisted milling is widely applied to typical difficult-to-machine materials, with its main advantages including reduced cutting force [18–19], improved surface quality[20–23], and suppressed tool wear[24–25]. Regarding the mechanism of intermittent cutting in ultrasonic vibration, researchers have mainly characterized the tool–workpiece separation and contact states in terms of contact ratio, net cutting time, and non-cutting time ratio. Ling Z et al.[26] varied parameters such as frequency and cutting speed to generate different cutting speed ratios k, and investigated the influence of UEVC separation characteristics on the cutting force and surface morphology during Ti-6Al-4V cutting under different k values. Wang X et al.[27] proposed a non-cutting time ratio model to predict the maximum reduction in milling force achievable by LUVM. Jian S et al.[28] established a kinematic model of the tool tip under ultrasonic

vibration assistance and analyzed the tool tip trajectory and chip separation law. Huang Z et al.[29] proposed partially separated continuous high-speed ultrasonic vibration cutting (C-HUVC). This method partially opens the cutting zone during continuous cutting, thereby resolving the contradiction between opening the cutting zone and improving the material removal rate (MRR) in ultrasonic vibration-assisted cutting (UVAC).

The above studies collectively indicate that the periodic separation between the tool and workpiece is an important kinematic feature distinguishing UVAM from conventional milling, and is also a key factor affecting cutting force, chip morphology, and surface quality. Current research on ultrasonic vibration separation characteristics still requires further refinement in terms of quantitative characterization and mechanism correlation. Existing indicators (e.g., contact ratio) are mostly used as qualitative aids; a kinematic model that takes separation time as a variable and explicitly relates it to feed speed v_f has not yet been established, and a unified dimensionless characterization method is lacking, making it difficult to theoretically elucidate the influence of v_f on cutting force, chip morphology, and tool wear. In addition, research on the ultrasonic separation behavior of TC11 titanium alloy under $scCO_2$-MQL conditions remains to be further improved. To address these issues, this paper focuses on the separation characteristics of TC11 titanium alloy during UVAM under $scCO_2$-MQL conditions. A separation kinematic model for a four-flute milling cutter is established, the separation ratio R_s is defined, and the separation time t_s is derived. Through finite element simulation and experimental verification, the effects of feed speed v_f on t_s, R_s, cutting force, chip morphology, and tool wear are investigated, and the accuracy of the model is validated, thereby providing a theoretical basis for high-efficiency and precision machining of TC11 titanium alloy.

2 Kinematic Modeling of Tool–Workpiece Separation in Ultrasonic Vibration-Assisted Milling

To quantitatively characterize the separation behavior in ultrasonic vibration-assisted machining, this chapter establishes a separation motion model between a four-flute milling cutter and the workpiece for ultrasonic vibration-assisted milling of TC11 titanium alloy under $scCO_2$-MQL conditions.

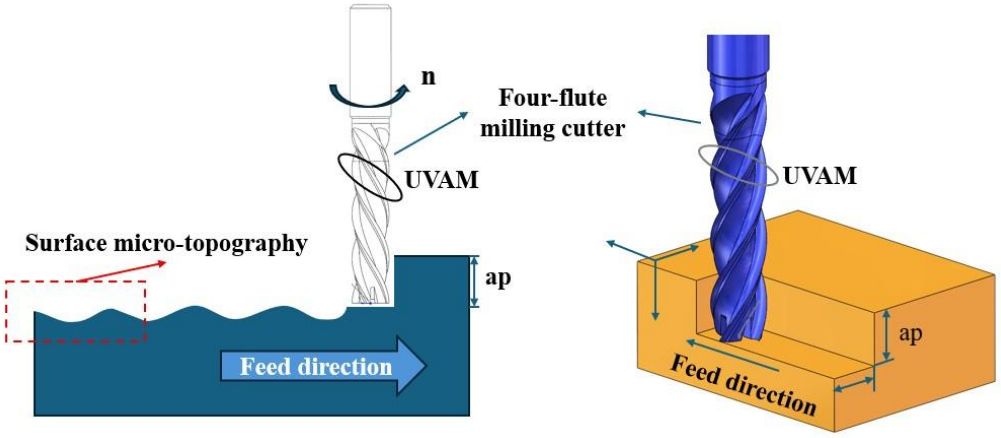

Fig. 2.1 Schematic diagram of milling

2.1 Establishment of the Tool Motion Trajectory Model

Let the motion trajectories of the i-th and (i+1)-th cutting edges be expressed as:

The i-th cutting edge:

$$x_i(t)=v_f t+A\sin(2\pi ft+\varphi)+R\cos(\omega t+\varphi_0) \tag{1}$$

$$y_i(t)=R\sin(\omega t+\varphi_0) \tag{2}$$

The (i+1)-th cutting edge (with a phase difference of π/2):

$$x_{i+1}(t)=v_f t+A\sin(2\pi ft+\varphi)+R\cos(\omega t+\varphi_0+\frac{\pi}{2}) \tag{3}$$

$$y_{i+1}(t)=R\sin(\omega t+\varphi_0+\frac{\pi}{2}) \tag{4}$$

The temporal interval between adjacent cutting edges (i.e., the time required for the tool to rotate through π/2):

$$\triangle t=\frac{\pi}{2\omega} \tag{5}$$

The actual uncut chip thickness is defined as:

$$h(t)=x_i(t)-x_{i+1}(t-\frac{\pi}{2\omega}) \tag{6}$$

Substituting the respective expressions and expanding the equations yields:

$$h(t)=\frac{v_f\pi}{2\omega}+A[\sin(2\pi ft+\varphi)-\sin(2\pi f(t-\frac{\pi}{2\omega})+\varphi)] \tag{7}$$

When the cutting thickness h(t)≤0, the tool and workpiece separate. Let the thickness variation induced by the vibration term be expressed as:

$$\triangle h_{vib}=2A\sin(\frac{\pi^2 f}{2\omega})\cos(2\pi ft+\varphi-\frac{\pi^2 f}{2\omega}) \tag{8}$$

Accordingly, the complete expression for the cutting thickness is given by:

$$h(t)=\frac{\pi v_f}{2\omega}+2A\sin(\frac{\pi^2 f}{2\omega})\cos(2\pi ft+\varphi-\frac{\pi^2 f}{2\omega}) \tag{9}$$

where:

$$\theta=\omega t+\varphi_0 \tag{10}$$

Let: $H_0=\frac{\pi v_f}{2\omega}$, $H_1=2A\sin(\frac{\pi^2 f}{2\omega})$

Then, the cutting thickness is simplified to:

$$h(t)=H_0+H_1\cos(2\pi ft+\varphi-\frac{\pi^2 f}{2\omega}) \tag{11}$$

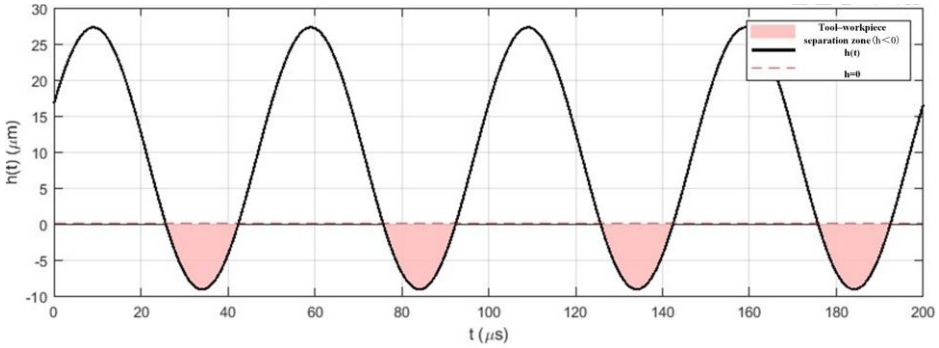

Fig. 2.2 Separation time

The separation parameter k is defined;

$$k=\frac{H_0}{H1}=\frac{\frac{\pi v_f}{2\omega}}{2A\sin(\frac{\pi^2 f}{2\omega})}=\frac{\pi v_f}{4\omega A\sin(\frac{\pi^2 f}{2\omega})} \tag{12}$$

From the definition of k, it can be seen that k is a dimensionless parameter governing the tool–workpiece separation behavior. The ultrasonic frequency f, amplitude A, tool angular velocity ω, and feed speed v_f all influence the value of k.

Then, the separation condition $h(t)\leq 0$ becomes:

$$\cos(2\pi ft+\varphi-\frac{\pi^2 f}{2\omega})=-k \tag{13}$$

To ensure the separation condition, the following condition must be satisfied:

$$|k|\leq 1 \tag{14}$$

that is：

$$\frac{\pi v_f}{4\omega A\sin(\frac{\pi^2 f}{2\omega})}\leq 1 \tag{15}$$

When $|k|\leq 1$, the times corresponding to the two separation boundary points are:

$$t_{s1}=\frac{\arccos(-k)-\varphi+\frac{\pi^2 f}{2\omega}}{2\pi f} \tag{16}$$

$$t_{s2}=\frac{2\pi-\arccos(-k)-\varphi+\frac{\pi^2 f}{2\omega}}{2\pi f} \tag{17}$$

The separation time interval is given by:

$$t_s=t_{s2}-t_{s1}=\frac{\arccos(k)}{\pi f}=\frac{1}{\pi f}\arccos\left(\frac{\pi v_f}{4\omega A\sin\left(\frac{\pi^2 f}{2\omega}\right)}\right) \tag{18}$$

The separation ratio is defined as:

$$R_s=\frac{t_s}{T}=t_s f \tag{19}$$

Substituting into Eq. (18):

$$R_s=\frac{1}{\pi}\arccos(k) \tag{20}$$

Therefore, R_s can serve as a key indicator for evaluating the degree of intermittent cutting in ultrasonic vibration-assisted milling. A larger R_s indicates a higher proportion of tool–workpiece separation time, more opportunities for the cooling–lubricating medium to enter the cutting zone, and thus greater potential for reducing the average cutting force and surface roughness and mitigating tool wear.

2.2 Maximum Separation Gap and Effective Cooling Time

In ultrasonic vibration-assisted milling, the periodic separation between the tool and workpiece is a prerequisite for scCO₂-MQL to exert its cooling and lubrication effects. When the uncut chip thickness satisfies $h(t)\leq 0$, a separation gap forms between the tool flank face and the machined surface, providing a channel for the cooling–lubricating medium to enter the cutting zone. During the separation phase, the instantaneous gap between the tool and workpiece can be expressed as:

$$g(t)=-h(t)=-H_0-H_1\cos\left(2\pi ft+\varphi-\frac{\pi^2 f}{2\omega}\right) \tag{21}$$

The maximum separation gap is reached when $\cos\left(2\pi ft+\varphi-\frac{\pi^2 f}{2\omega}\right)=-1$:

$$g_{max}=H_1-H_0=H_1(1-k) \tag{22}$$

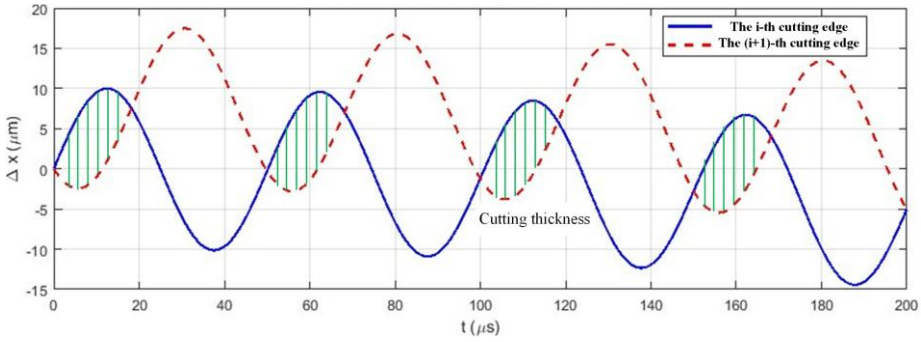

Fig. 2.3 Uncut chip thickness

The maximum separation gap g_{max} determines the channel width for the cooling–lubricating medium to enter the cutting zone. As the feed speed v_f increases, k

increases and g_{max} decreases; consequently, the channel for the medium narrows and the cooling–lubrication effect deteriorates.

The effective cooling time for scCO₂-MQL to enter the cutting zone is proportional to the separation time:

$$t_{cool}=\eta \cdot t_s \tag{23}$$

where η is the penetration coefficient of the cooling medium ($0<\eta\leq1$), which depends on the nozzle position, injection angle, and separation gap width. Combining Eq. (22), η can be further expressed as a function of g_{max}:

$$\eta=\eta_0 \cdot \frac{g_{max}}{g_{max}+g_0} \tag{24}$$

where η_0 is the ideal penetration coefficient, and g_0 is the characteristic gap width, defined as the characteristic droplet diameter of the scCO₂ aerosol or the critical gap for capillary penetration, taken as $g_0=15$ μm.Combining the above equations, it follows that:

$$t_{cool}=\eta_0 \cdot \frac{H_1(1-k)}{H_1(1-k)+g_0} \cdot \frac{1}{\pi f}\arccos(k) \tag{25}$$

According to Eq. (25), the following trend is obtained: an increase in feed speed v_f increases k, which, on the one hand, shortens the separation time t_s and, on the other hand, reduces the maximum separation gap g_{max}. These two effects jointly cause the effective cooling time t_{cool} to decrease significantly. This implies that at a higher feed speed, not only is the separation effect itself weakened, but the conditions for the cooling–lubricating medium to enter the cutting zone also deteriorate simultaneously; consequently, the potential of the separation effect to improve machining quality is doubly weakened.

3 Finite Element Simulation of Ultrasonic Vibration-Assisted Milling

In this chapter, a three-dimensional simulation model of ultrasonic vibration-assisted milling of TC11 titanium alloy is established using the Abaqus finite element software. The model aims to validate the separation motion model developed in Chapter 2 from kinematic and mechanical perspectives, and to reveal the influence of feed speed v_f on the separation time t_s, separation ratio R_s, cutting force, and chip morphology.

3.1 Establishment of the Johnson–Cook Constitutive Model for TC11 Titanium Alloy

$$\bar{\sigma}=\left[A+B\left(\bar{\varepsilon}^{pl}\right)^{n}\right]\left[1+C\ln\left(\frac{\dot{\bar{\varepsilon}}^{pl}}{\dot{\varepsilon}_0}\right)\right]\left[1-\left(\frac{T-T_0}{T_m-T_0}\right)^{m}\right]$$

Where $\bar{\varepsilon}^{pl}$ is the equivalent plastic strain, $\dot{\bar{\varepsilon}}^{pl}$ is the equivalent plastic strain rate, T_m is the melting temperature of the material, and T_0 is the reference temperature, usually taken as room temperature. A is the yield strength, B and n are the strain hardening parameters, C is the strain rate sensitivity coefficient, and m is the thermal softening exponent[30].

Table 3.1 Material coefficients

A	B	C	n	m	melting temperature
1098	793	0.01	0.386	0.71	1560℃

3.2 Simulation Environment and 3D Model Construction

A three-dimensional milling simulation was performed using Abaqus 2024. Based on the experimental requirements, a simplified three-dimensional model was established. The milling cutter has a diameter of 10 mm and a height of 80 mm, and the workpiece is a rectangular block with dimensions of 20×15×7.5 mm. The three-dimensional model was simplified as follows:

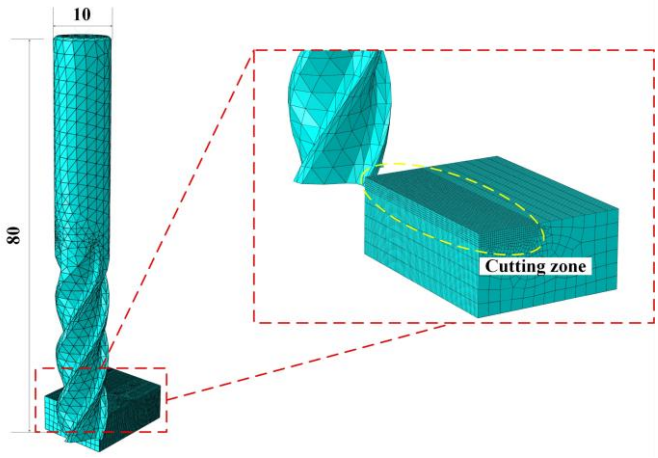

Fig. 3.1 Assembly model and mesh generation

The tool was defined as a rigid body, and the workpiece was modeled as an elastoplastic deformable body. Tie constraints were applied to the cutting region and the workpiece substrate, and rotational and translational loads were applied to the entire tool to realistically simulate the actual tool motion. Tetrahedral elements were used for both the milling cutter and the workpiece, with a total of 43,100 elements. Dynamic explicit analysis was adopted with an analysis time of 1 s, and a mass scaling factor of 200 was used to ensure computational efficiency. The conventional penalty contact method was employed for contact interactions.

Table 3.2 Comparison of simulation speeds

v_c(m/min)	f_z(mm/z)	v_f(mm/min)	simulation validation
50		318.3	low cutting speed
75	0.05	477.5	medium cutting speed
100		636.6	high cutting speed

To simulate the cooling and lubrication effects of scCO₂-MQL, equivalent thermal boundary conditions were adopted in the coupled thermal–mechanical model in Abaqus. An equivalent convective heat transfer coefficient h was applied to the tool–chip and tool–workpiece contact zones, with a value of 18200W·(m^{-2}·K^{-1}), to reflect the high permeability and enhanced heat transfer characteristics of scCO₂[25].

3.3 Simulation Results

To systematically validate the influence of v_f on t_s, R_s, and the machining performance in the theoretical model, this section analyzes three aspects: cutting force, chip morphology, and cutting temperature.

(1) According to the separation model, as v_f increases, k increases, while t_s and R_s decrease. Consequently, the tool–workpiece contact time per unit time increases, the separation effect weakens, and the average cutting force therefore increases. In the figure, the 50m/min curve is the lowest overall, whereas the 75 and 100m/min curves are generally higher, with markedly increased peak values.

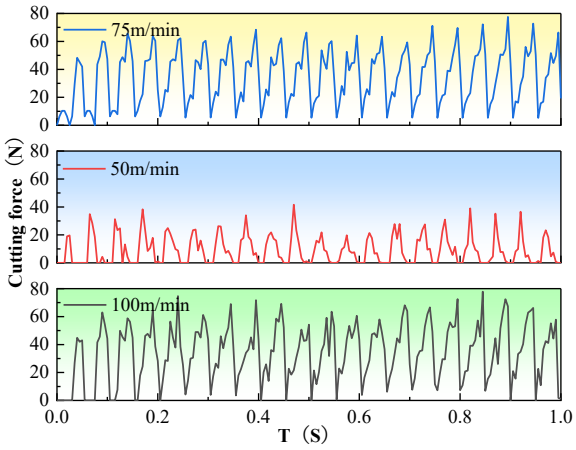

Fig. 3.2 Comparison of simulated cutting forces

As the cutting speed increases from 50 to 100m/min, the cutting force exhibits an overall upward trend. Under ultrasonic vibration, the cutting force curves show high-frequency fluctuations and periodic zero-value intervals, indicating periodic separation between the tool and workpiece.

(2) With increasing feed speed v_f, the chips change from discontinuous chips to

relatively long C-shaped chips. The discrete, short fragmented chips in Fig. 3.3(a), compared with those in Fig. 3.3(b) and (c), further indicate that as v_f increases, the chips transform from discontinuous chips into C-shaped chips and then into long spiral ribbon-like chips. When v_f changes, a smaller v_f leads to a longer separation time, a larger R_s, a larger g_{max}, and a longer t_{cool}, resulting in a higher chip breakage frequency and shorter chips.

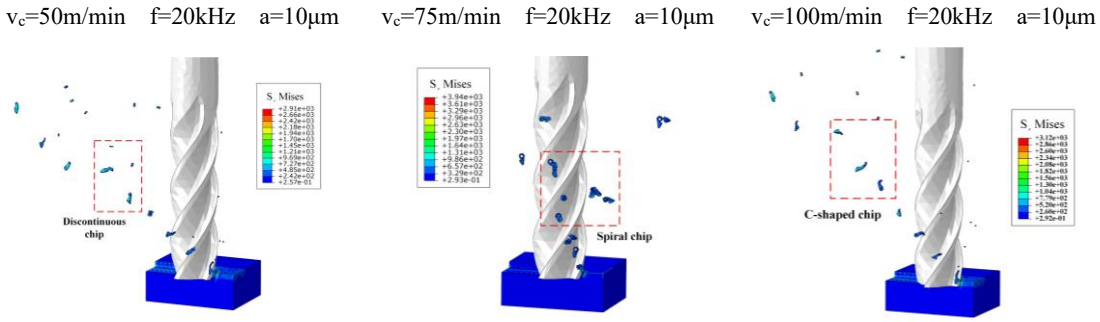

Fig. 3.3 Comparison of chip morphologies

(3) As the feed speed v_f increases, the separation parameter k increases accordingly, which reduces the separation ratio R_s, narrows the maximum separation gap g_{max}, and significantly shortens the effective cooling time t_{cool} for the cooling medium to enter the cutting zone. This theoretical trend is directly corroborated by the simulated temperature field: the deterioration of the cooling channel at high speed leads to heat accumulation, causing the cutting temperature at 100m/min (approximately 450 °C) to be higher than that at 50m/min (approximately 440 °C). Similarly, in the experiments, the weakened separation effect also leads to a smaller reduction in cutting force, less improvement in surface roughness, and a higher tool wear rate at high speeds.

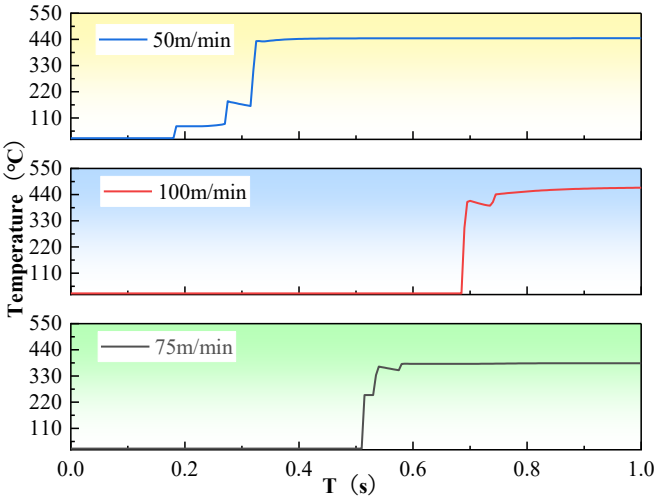

Fig. 3.4 Comparison of simulated cutting temperatures

In summary, the simulation results show that as the feed speed v_f increases, the cutting

force increases overall, the zero-value separation intervals shorten, the chips transform from short C-shaped chips into long ribbon-like chips, and the cutting temperature tends to rise. These trends are consistent with the theoretical model, which predicts that an increase in v_f increases the separation parameter k and decreases the separation time t_s and separation ratio R_s. The simulation results and the theoretical model corroborate each other, thereby validating the established separation motion model.

Because the finite element model did not fully couple the hydrodynamic pressure effect of $scCO_2$ fluid scouring and a mass scaling factor of 200 was adopted to improve computational efficiency, the simulated peak forces are slightly higher than the measured values. Nevertheless, the simulation and experimental results exhibit highly consistent trends with varying speed, confirming the qualitative accuracy of the model.

4 Experimental Study on Ultrasonic Vibration-Assisted Milling

4.1 Experimental Materials, Cutting Tools, and Equipment

The base material used in the experiments was TC11 titanium alloy bar stock (Ti–6.5Al–3.5Mo–1.5Zr–0.3Si). This alloy exhibits both high mechanical strength and good creep resistance at medium and elevated temperatures and is therefore widely used in the aerospace field. Its key physical and mechanical properties are listed in the following table:

Table 4.1 Physical and mechanical properties of TC11 titanium alloy

parameter	value
ρ（g/cm^3）	4.48
σs（MPa）	≥900
E（GPa）	120
λW/（m·K）	6.7

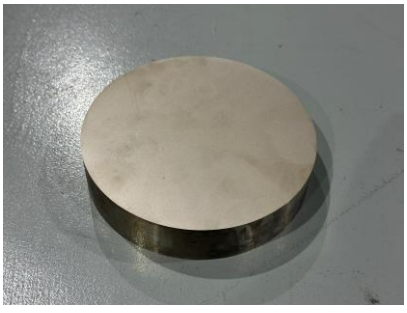

Fig. 4.1 TC11 titanium alloy

The experimental platform was a CAM-UWV-850M CNC ultrasonic three-axis machining center equipped with a Huazhong HNC-808D CNC system. A TC11 titanium alloy bar with a diameter of 140 mm was selected as the workpiece and mounted on a fixture.



Fig. 4.2 Machine tool spindle

A coated cemented carbide cutting tool was selected, namely a JDR four-flute milling cutter with a TiAl/TiSi coating. The cutter was mounted in a tool holder and secured in the fixture to ensure smooth experimental operation. The ultrasonic vibration frequency was 20 kHz, and the amplitude was 10 μm.

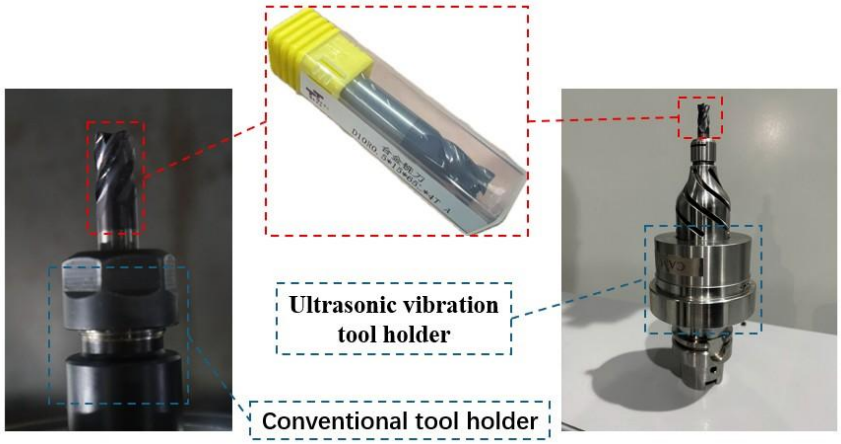

Fig. 4.3 Tool holder and cutting tool

In this study, two auxiliary machining processes were investigated: $scCO_2$-MQL alone and $scCO_2$-MQL combined with ultrasonic vibration. For $scCO_2$-MQL alone, the cutting tool was clamped in a conventional tool holder. A 6% emulsion was used as the cutting fluid and supplied by a separate MQL pump. The $scCO_2$ and the cutting fluid were delivered through two high-pressure rubber hoses to the ends of high-pressure nozzles mounted on the tool turret.

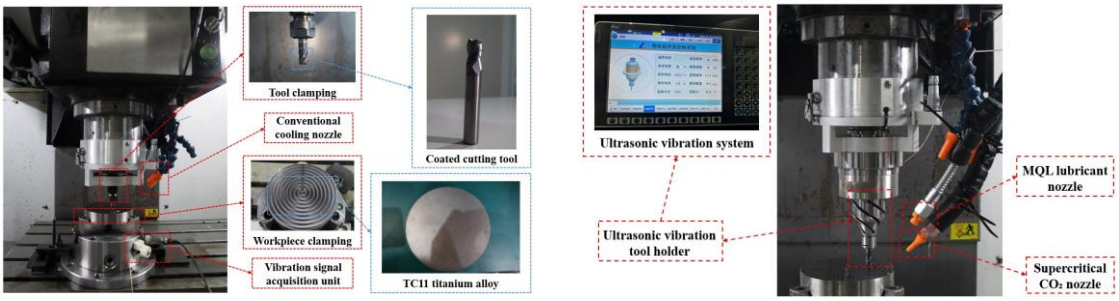

(a) Conventional machining setup **(b) Ultrasonic vibration setup**

Fig. 4.4 Comparison of machine tool configurations

For $scCO_2$-MQL combined with ultrasonic vibration, an ultrasonic vibration tool holder was used. This tool holder converts the ultrasonic electrical signal into high-frequency mechanical vibration through an integrated piezoelectric transducer and transmits the vibration to the cutting tool. The ultrasonic vibration frequency was set to 20 kHz, and the amplitude was 10 μm. The cooling and lubrication configuration was identical to that of $scCO_2$-MQL alone. The nozzle diameter was also 1.3 mm, and the spray angle was adjusted so that the mixed aerosol was precisely directed at the milling cutter tip, ensuring its effective entry into the cutting zone under ultrasonic vibration.

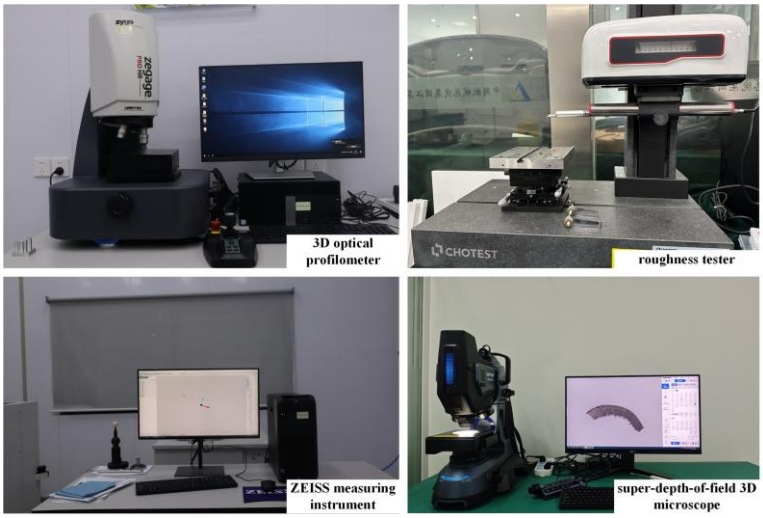

Fig. 4.5 Experimental equipment

Cutting forces were measured with a Kistler 9272 dynamometer (Switzerland) connected to a matching charge amplifier, which converted the charge signal into a voltage signal. The signals were recorded and post-processed using the DynoWare data acquisition and analysis software. The machined surface roughness was measured non-contactly by a white-light interferometer at three different positions on each surface, and the average roughness Ra was taken as the evaluation index. The chip morphology and tool wear morphology were observed using a super-depth-of-field microscope

(DMI1000), and the surface elemental distribution was analyzed in combination with the white-light interferometer.

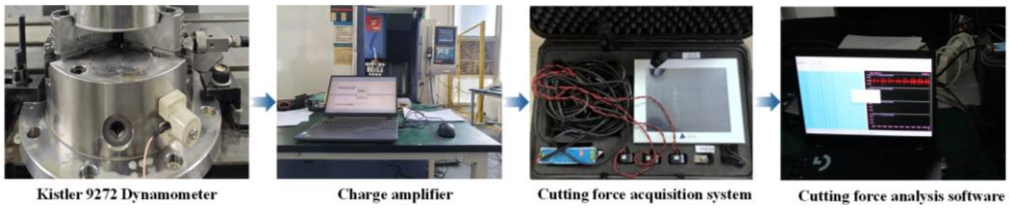

Fig. 4.6 Force and vibration signal measurement system

4.2 Design of the Experimental Scheme

To systematically investigate the influence of feed speed v_f on the separation characteristics and machining performance, a full factorial experimental design was adopted. Three factors were considered: cutting speed v_c(50, 75, and 100 m/min), axial depth of cut a_p(0.1 and 0.3 mm), and cooling–lubrication method (scCO₂-MQL、scCO₂-MQL combined with ultrasonic vibration). The feed per tooth f_z was fixed at 0.05mm/z, so that v_f increased with increasing v_c. According to the full factorial design, a total of $3 \times 2 \times 2 = 12$ experimental conditions were constructed to comprehensively evaluate the main effects and interactions of the factors.

Table 4.2 Experimental parameters

process parameters	values
v_c(m/min)	50、75、100
f_z（mm/z）	0.05
a_p（mm）	0.1、0.3
cooling method	scCO₂-MQL、scCO₂-MQL+UVAM

The cylindrical material was divided equally into eight cutting zones of equal area, so that the cutting path length, cutting edge engagement time, and cutting-layer geometric parameters remained highly consistent within each zone. Consequently, the cutting load, cutting heat generation, and tool wear rate were equivalent among the eight zones.

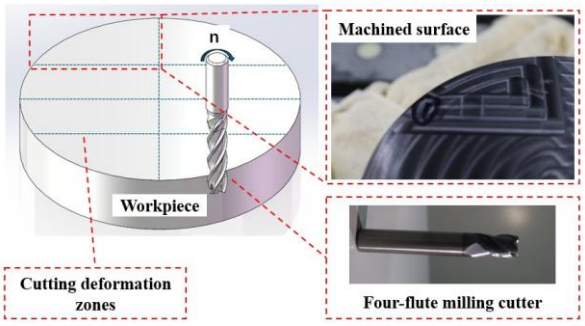

Fig. 4.7 Milling toolpath

5 Analysis of Experimental Results

Two cooling–lubrication conditions were employed in the experiments: scCO₂-MQL alone and scCO₂-MQL combined with ultrasonic vibration (hybrid process). This section focuses on comparatively analyzing the effects of feed speed v_f on cutting force, surface roughness, tool wear, and chip morphology under the two process conditions.

5.1 Cutting Force Analysis

As shown in Fig. 5.1, when the cutting speed increased from 50 to 100 m/min, the cutting force increased under both cooling–lubrication conditions. The cutting force under the hybrid process remained consistently lower than that under scCO₂-MQL alone, and the reduction decreased with increasing cutting speed, with values of 26%, 13%, and 10% at 50, 75, and 100 m/min, respectively. This indicates that the separation-induced force reduction is more pronounced at low cutting speeds.

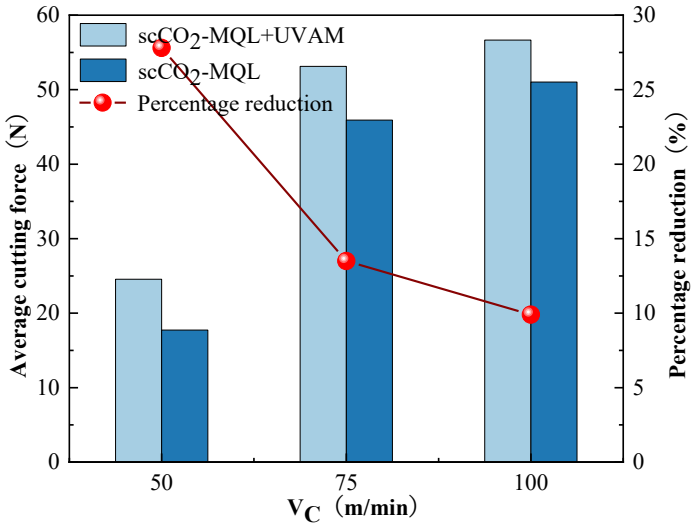

Fig. 5.1 Comparison of average cutting forces

This trend is consistent with the separation motion model. At a lower feed speed v_f, the separation time t_s is longer and the separation ratio R_s is larger, so that the tool and workpiece separate sufficiently, allowing scCO₂-MQL to enter the cutting zone more easily and thereby producing a pronounced force reduction. As v_f increases, the separation parameter k increases, while t_s and R_s decrease; consequently, the tool–workpiece separation effect weakens, scCO₂-MQL becomes less able to enter the cutting zone, and the force reduction magnitude of the hybrid process decreases with increasing speed.

5.2 Machined Surface Quality

As shown in Fig. 5.2, when the cutting speed increased from 50 to 100 m/min, the

surface roughness Ra generally increased under both scCO₂-MQL alone and the hybrid process. However, the Ra under the hybrid process remained consistently lower than that under scCO₂-MQL alone: the Ra values under scCO₂-MQL alone were approximately 0.412, 0.409, and 0.465 μm, whereas those under the hybrid process were approximately 0.185, 0.231, and 0.269 μm, corresponding to reductions of approximately 55%, 44%, and 42%, respectively. That is, the reduction decreased with increasing cutting speed, indicating that ultrasonic vibration more markedly improves surface quality at low speeds. This mechanism agrees with the separation motion model: at a lower feed speed v_f, the separation time t_s is longer and the separation ratio R_s is larger, allowing scCO₂-MQL to enter the cutting zone more easily; as v_f increases, t_s shortens and R_s decreases, the separation effect weakens, and the improvement in surface quality accordingly diminishes.

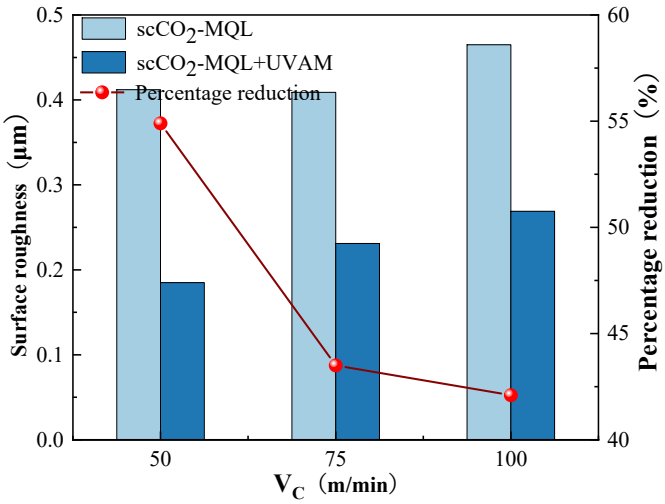

Fig. 5.2 Comparison of surface roughness

As shown in Fig. 5.3, under scCO₂-MQL alone, the surface is dominated by continuous network-like scratches, whereas under the hybrid process, it exhibits a uniformly modulated texture. This change is related to the separation time: at a lower feed speed v_f, the separation time t_s is longer and the separation ratio R_s is larger, so that the scCO₂-MQL medium penetrates the tool–workpiece interface more sufficiently, and both scale-like burr formation and flank-face friction are suppressed. As v_f increases, t_s shortens accordingly, the separation becomes insufficient, and the improvement in the machined surface quality decreases. In the simulation, an increase in R_s shifts the surface-layer residual stress toward a compressive state, which also supports this result.

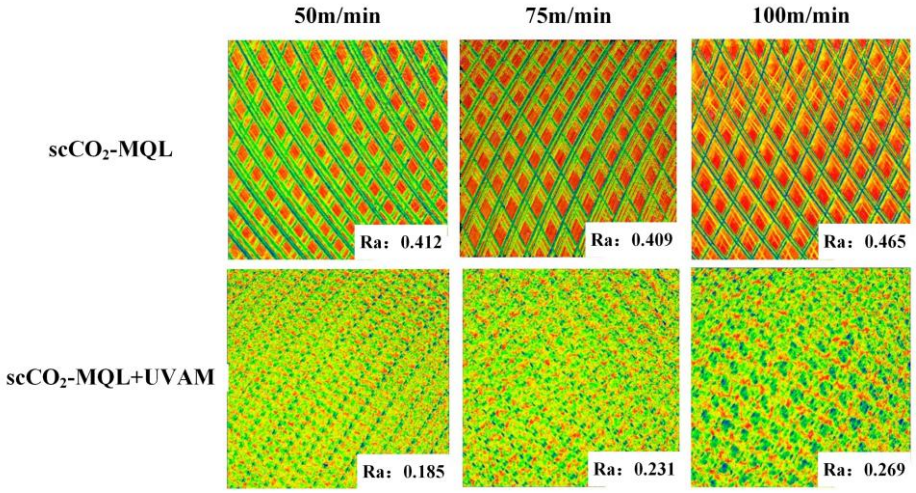

Fig. 5.3 Comparison of machined surface morphologies

This is consistent with the theoretical model in Chapter 2: at low speeds, the feed speed v_f is smaller, k is smaller, R_s is larger, the maximum separation gap g_{max} is larger, and the effective cooling time t_{cool} is longer, so that scCO₂-MQL can more fully enter the cutting zone and thereby suppress scale-like burr formation and flank-face friction. As v_f increases, k increases, while R_s, g_{max}, and t_{cool} all decrease; consequently, the separation effect and the cooling–lubrication conditions deteriorate simultaneously, and the improvement in surface quality diminishes accordingly.

5.3 Tool Wear Analysis

As shown in Figs. 5.4 and 5.5, the wear width under the two processes was comparable at 12 min. After 24 min, the wear width under the hybrid process remained consistently lower than that under scCO₂-MQL alone: 74.52 μm versus 140.32 μm at 36 min and 150.16 μm versus 365.93 μm at 48 min, with a reduction of approximately 60% at 48 min. The wear morphology also changed from abrasive–adhesive wear to mild, uniform polishing wear. This is because a larger R_s shortens the actual tool–chip contact time and lowers the mechanical and thermal loads in the cutting zone, thereby suppressing built-up edge formation and abrasive cutting. In the simulated contour plots in Fig. 3.3, the increase in feed speed v_f and the separation effect periodically interrupt chip formation, causing the chips to change from discontinuous chips to short C-shaped chips; a larger R_s leads to a higher chip-breaking frequency and shorter chips, indirectly indicating a reduction in tool–chip contact time, which is consistent with the experimentally observed reduction in tool wear.

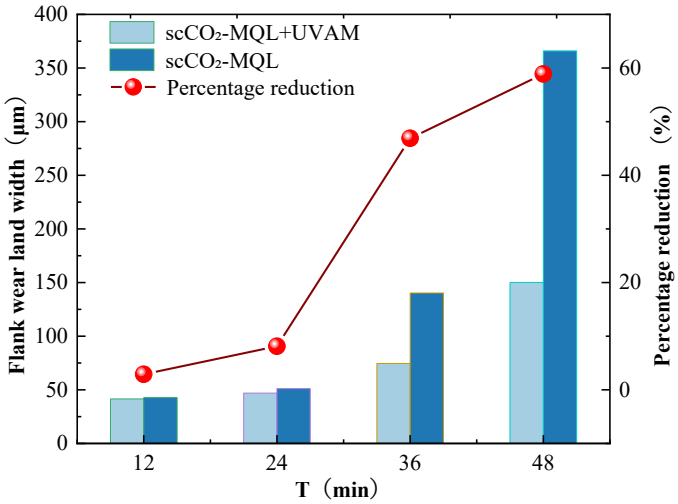

Fig 5.4 Tool wear width

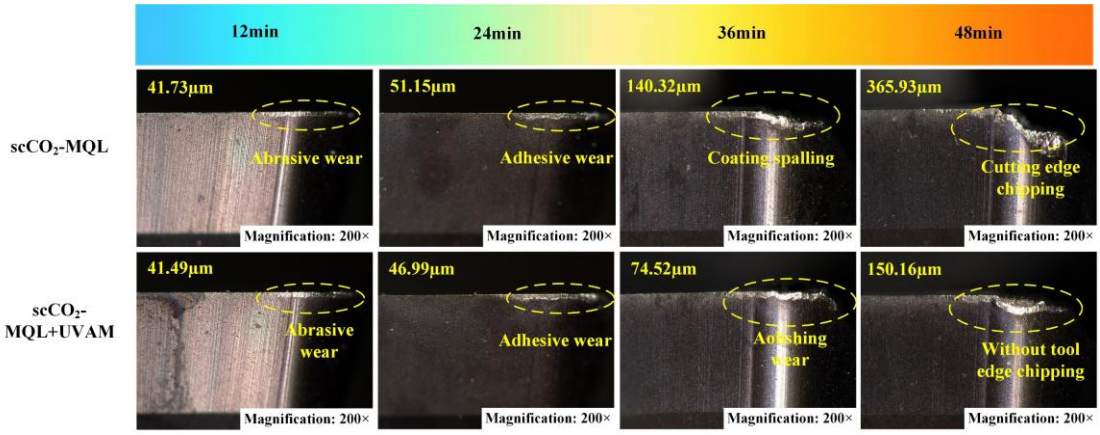

Fig. 5.5 Comparison of tool wear

According to the model in Chapter 2, a larger R_s shortens the actual tool–chip contact time and lowers the mechanical and thermal loads in the cutting zone, thereby more effectively suppressing built-up edge formation and abrasive cutting. As the feed speed v_f increases, k increases and R_s decreases; although the suppression effect of separation on tool wear is somewhat weakened, the hybrid process still performs significantly better than scCO₂-MQL alone. This indicates that the separation ratio R_s is a key theoretical indicator for explaining the differences in tool wear.

5.4 Chip Morphologies

As the cutting speed increased from 50 to 100 m/min, the feed speed v_f increased accordingly, and the chip morphology gradually changed from discontinuous chips and short C-shaped chips at low speed to long spiral ribbon-like chips. The chip length increased from 1000 to 6000 μm, while the chip-breaking frequency decreased, resulting in deteriorated chip evacuation.

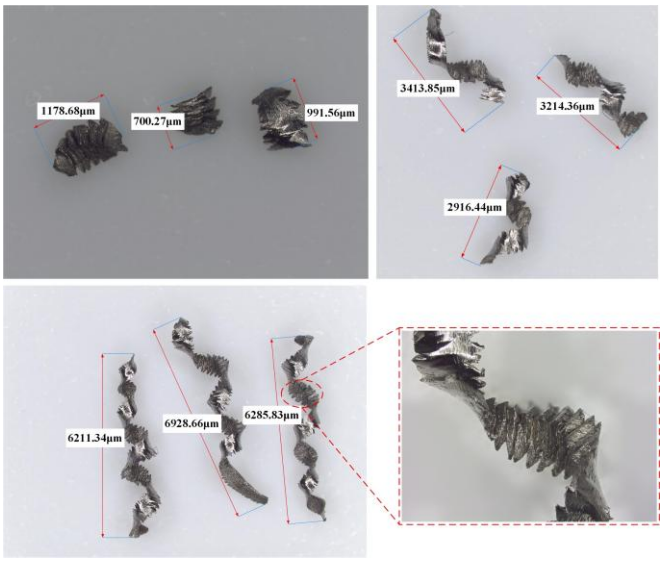

Fig. 5.6 Comparison of chip morphologies

This phenomenon is consistent with the theoretical model in Chapter 2: as the feed speed v_f increases, the separation parameter k increases, while the separation time t_s and separation ratio R_s decrease. Consequently, the tool–workpiece separation becomes insufficient, the continuous tool–chip contact time is prolonged, and the periodic interruption of chips is weakened. Therefore, a larger R_s corresponds to shorter chips and a higher chip-breaking frequency, whereas a smaller R_s corresponds to longer chips that are more likely to form spiral ribbons. The evolution of chip morphology not only reflects the strength of the separation effect but can also serve as an intuitive indicator for assessing changes in machining quality during ultrasonic vibration-assisted milling.

6 Conclusions

Combining theoretical derivation, finite element simulation, and experimental validation, the main conclusions of this study are as follows:

(1) Construction of the separation motion theoretical model. Based on a four-flute milling cutter, a separation–contact model for ultrasonic vibration-assisted milling was established, and the relationships between the feed speed v_f and the separation time t_s, separation ratio R_s, and maximum separation gap g_{max} were derived. R_s and g_{max} characterize the separation behavior from two dimensions—temporal proportion and spatial channel—thereby providing a theoretical basis for the subsequent analysis of cutting performance evolution.

(2) The separation characteristics regulate the cutting force. The average cutting force

under the hybrid process was consistently lower than that under $scCO_2$-MQL alone, and the reduction decreased with increasing feed speed v_f. The analysis indicates that an increase in v_f causes R_s and the effective cooling time t_{cool} to decrease simultaneously, thereby weakening the periodic separation effect and the cooling–lubrication conditions.

(3) The separation motion effectively improved the surface integrity. The surface roughness Ra under the hybrid process was consistently better than that under $scCO_2$-MQL alone, and the improvement was more pronounced at low speeds. At low speeds, the larger R_s and longer t_{cool} ensured deep penetration of $scCO_2$-MQL into the cutting zone and suppressed scale-like burr formation. As v_f increased, the simultaneous attenuation of the separation and cooling effects limited the improvement in surface quality.

(4) Suppression of tool wear by the separation motion. After 24 min, the tool wear width under the hybrid process remained consistently lower than that under $scCO_2$-MQL alone, and the wear morphology changed from severe abrasive–adhesive wear to mild, uniform polishing wear. Theoretical analysis indicates that a larger R_s shortens the actual tool–chip contact time, thereby effectively suppressing built-up edge formation and the micro-plowing action of abrasive particles.

In summary, the separation motion model developed in this study elucidates how v_f governs R_s and t_{cool}. Simulations and experiments verified the role of the separation characteristics in reducing the cutting force, improving surface integrity, and alleviating tool wear, thereby establishing R_s as a key indicator for evaluating the degree of intermittent cutting in UVAM. These results provide a theoretical basis for rationally matching process parameters to maintain a relatively high R_s and fully exploit the separation effect and the synergistic cooling advantage of $scCO_2$-MQL.

Funding: National Natural Science Foundation of China, Grant No. 52265059
Research Startup Fund for High-level Talents of Tianshui Normal University, Grant No. Tsnu2026021

Declarations

Conflict of Interest

The authors declared no potential conflict of interest with respect to the research, authorship, and/or publication of this article.

Author contributions

Limin Shi: Writing-original draft, Visualization, Formal analysis, Conceptualization, Data- curation, Supervision, Funding acquisition. Haonan Chen: Data curation, Formal analysis, Visualization, Writing-origin draft. Lixin Cui: Visualization, Investigation, Software. Yifan Zhang: Visualization, Data curation, Investigation. Ronghuan Liu: Writing-review & editing, Methodology, Formal analysis. Nana Li and Deguo Kong: Conceptualization, Project administration, Writing-review & editing. All authors commented on previous versions of the manuscript. All authors read and approved the final manuscript.

References

[1] Chai Z ,Wang Y W ,Ren Y , et al.Hot deformation behavior and microstructure evolution of TC11 dual-phase titanium alloy[J]. Materials Science & Engineering A,2024,898146331-.

[2] Xiang B ,Zhang P ,Han P , et al.Microstructural evolution and mechanical properties of TC11 titanium alloy during α+β hot deformation[J]. Journal of Materials Research and Technology, 2025 ,397429-7439.

[3] Li Z ,He Y ,Cao Y , et al.Analysis of grinding temperature and grinding surface quality in ultrasonic vibration-assisted grinding of GH4169 superalloy based on Welch-Type heat source distribution[J]. The International Journal of Advanced Manufacturing Technology, 2026 ,144(7-8):1-15.

[4] Yi-Jia S ,Hu G ,Shu-Yu G , et al.Towards understanding the cutting temperature in ultrasonic vibration-assisted drilling based on the dynamic contact characteristics between the cutting edge and workpiece[J]. Ultrasonics,2023,135107131-107131.

[5] Chen S ,Zhang B ,Teng H , et al.Modeling of tool wear and life prediction in ultrasonic vibration-assisted blade dicing[J]. Journal of Manufacturing Processes, 2026 ,175877-891.

[6] Zhang C ,Li H ,Zhang X , et al.Parameter optimization, machining quality, removal mechanism, and tool wear in ultrasonic-vibration-assisted micro-hole drilling process of Cf/SiC ceramic matrix composites[J]. Ceramics International, 2025 ,51(29PB):60645-60656.

[7] XIA Z ,SHAN C ,ZHANG M , et al.Machinability of elliptical ultrasonic vibration milling γ-TiAl: Chip formation, edge breakage, and subsurface layer deformation[J]. Chinese Journal of Aeronautics, 2025 ,38(3):103096-103096.

[8] Pascal F ,Ilgar A .Chip Formation and Shaping in Milling Machining of Light Metal Casting Materials[J].Key Engineering Materials, 2024 ,9793-10.

[9] Bashir A M ,Khan T ,Nair R .Evaluation of hydrophilicity and surface morphology of nanosecond-pulsed laser-engineered surface textures on stainless steel, cobalt-chromium, and titanium alloys[J]. Journal of Materials Science: Materials in Medicine, 2025 ,36(1):106-106.

[10] Rauf A ,Butt I S ,Jaffery I H S , et al.Statistical analysis of surface roughness in meso scale ultrasonic vibrations assisted end-milling (UVAEM) of titanium alloy Ti–6Al–4V under dry, flooded, MQL and cryogenic environments[J]. Journal of Materials Research and Technology, 2025 ,399721-9734.

[11] Wang H ,Wang C ,Dang J , et al.Frication behaviors, wear and failure mechanisms of CBN tool and machined surface morphology in high-speed turning of high strength refractory alloy cast steel[J]. Journal of Manufacturing Processes, 2025 ,138186-202.

[12] Ali A ,Younas M ,Khan M , et al.Machinability Performance of Single Coated and Multicoated Carbide Tools During Turning Ti6Al4V Alloy[J]. International Journal of Precision Engineering and Manufacturing, 2024 ,26(1):1-16.

[13] Trung C L ,Phuc T T .Performance of TiSiN/TiAlN-Coated Carbide Tools in Slot Milling of Hastelloy C276 with Various Cooling Strategies[J]. Lubricants, 2025 ,13(7):316-316.

[14] Zhang G ,Li H ,Deng Y , et al.Investigation of surface integrity in ultrasonic vibration-assisted minimum quantity lubrication milling of Ti-6Al-4V thin-walled parts[J]. The International Journal of Advanced Manufacturing Technology, 2026 ,143(1-2):1-13.

[15] Mehmood T ,Khalil S M .Enhancement of Machining Performance of Ti-6Al-4V Alloy Though Nanoparticle-Based Minimum Quantity Lubrication: Insights into Surface Roughness, Material Removal Rate, Temperature, and Tool Wear[J]. Journal of Manufacturing and Materials Processing, 2024 ,8(6):293-293.

[16] Khan A M ,Ali M B A ,Ullah S , et al.A review on recent advancements in ultrasonic vibration-assisted machining of difficult-to-machine materials[J]. International Journal on Interactive Design and Manufacturing (IJIDeM), 2025 ,19(12):1-36.

[17] Yu H ,Liang X ,Guo F , et al.Laser-ultrasonic vibration hybrid assisted machining in advanced difficult-to-cut materials: Technologies, mechanisms, and

challenges[J]. Journal of Materials Processing Tech., 2025 ,345119076-119076.

[18] Xie W ,Yan J ,Tie Y , et al.Surface Integrity Investigation into Longitudinal-Torsional Ultrasonic Vibration Side Milling for a TC18 Titanium Alloy—Part II: Effects of Ultrasonic Amplitude on Cutting Force and Surface Integrity[J]. Journal of Vibration Engineering & Technologies, 2025 ,13(6):383-383.

[19] Jieqiong L ,Chao W ,Mingming L , et al.Modeling and investigation of cuttingforce for SiCp/Al composites during ultrasonic vibration-assisted turning[J]. Proceedings of the Institution of Mechanical Engineers, Part E: Journal of Process Mechanical Engineering, 2022 ,236(3):1013-1022.

[20] CHANG B ,YI Z ,ZHANG F , et al.A comprehensive research on wear resistance of GH4169 superalloy in longitudinal-torsional ultrasonic vibration side milling with tool wear and surface quality[J]. Chinese Journal of Aeronautics, 2024 ,37(4):556-573.

[21] Jin Z ,Li L ,Yue Q W , et al.Surface quality investigation in high-speed dry milling of Ti-6Al-4V by using 2D ultrasonic-vibration-assisted milling platform[J]. Advances in Manufacturing, 2024 ,12(2):349-364.

[22] Wu Z ,Zhang D ,Li J , et al.Influence of milling-finishing-shot peening hybrid machining on the surface integrity and fatigue performance of TC11 titanium integral impeller[J]. The International Journal of Advanced Manufacturing Technology, 2024 ,(prepublish):1-11.

[23] Tian Y ,Cao H ,Yin S , et al.Study on surface quality in longitudinal-torsional composite ultrasonic vibration assisted drilling of CFRP/Ti stacks[J]. The International Journal of Advanced Manufacturing Technology, 2025 ,142(3-4):1-14.

[24] Chen G ,Wang J ,Xu J , et al.Effect of forward and reverse cutting on tool wear behavior in ultrasonic vibration-assisted milling of 3D needle-punched C/SiC composites[J]. Wear,2024,552-553205454-205454.

[25] Hao Z ,Zhang H ,Fan Y .Tool wear mathematical model of PCD during u ltrasonic elliptic vibration cutting SiCp/Al composite[J].International Journal of Refractory Metals and Hard Materials,2025,126106967-106967.

[26] Ling Z ,Wang D ,Wu S , et al.Effect of separation characteristics on cutting force and surface quality in ultrasonic elliptical vibration cutting of Ti-6Al-4V[J]. The International Journal of Advanced Manufacturing Technology, 2025 , (prepublish) :1-18.

[27] Wang X ,He Q ,Zhao B , et al.Material removal and surface texture in the longitudinal ultrasonic vibration-assisted milling of GH4169D superalloy[J]. Frontiers of Mechanical Engineering, 2025 ,20(2):13-13.

[28] Jian S ,Pengyang L ,Shen Z , et al.Experimental study of surface integrity in ultrasonic vibration–assisted milling of GH4169 nickel-based superalloy[J]. The International Journal of Advanced Manufacturing Technology, 2023 ,129(11-12):5047-5058.

[29] Huang Z ,Li J ,Zhang M , et al.Feasibility study of partial separation continuous high-speed ultrasonic vibration cutting Inconel 718[J]. Journal of Materials Research and Technology, 2025 ,352584-2601.

[30] Xiao G ,Yang B ,Sun H , et al.Study on microstructure evolution and unified viscoplastic constitutive model of TC11 titanium alloy during hot deformation based on shear-compression experiments[J]. Journal of Alloys and Compounds, 2026 ,1068188499-188499.